RSC Advances

PAPER

View Article Online
View Journal | View Issue

Cite this: *RSC Adv.*, 2021, **11**, 3547

Pseudo-octahedral nickel(II) complexes of strongly absorbing benzannulated pincer-type amido ligands: ligand-based redox and non-Aufbau electronic behaviour†

Jason D. Braun, [a] Issiah B. Lozada, [a] Michael Shepit,[b] Johan van Lierop [bc] and David E. Herbert *[ac]

Received 22nd December 2020
Accepted 7th January 2021

DOI: 10.1039/d0ra10761a

rsc.li/rsc-advances

The synthesis, structures and electronic characterization of three strongly coloured, pseudo-octahedral Ni(II) complexes supported by redox-active diarylamido ligands featuring benzannulated *N*-heterocyclic donor arms are reported. The $S = 1$ paramagnets each present two singly occupied molecular orbitals (SOMOs) identified as metal-based by density functional theory (DFT), consistent with solid-state and solution magnetism measurements. Upon applying oxidative potentials, non-Aufbau behaviour leads to the appearance of intense and well-defined absorption features extending into the near IR (NIR). The attribution of these features to the onset of aminyl radical character through ligand-based redox is corroborated by exceptionally strong intervalence charge-transfer (IVCT) transitions ascribed to electronic communication between two N_{amido} moieties across a Ni(II) bridge.

Introduction

Redox 'non-innocent' ligands have long been a topic of interest owing to their ability to imbue metal coordination complexes (MCCs) with unconventional physical properties[1,2] and reactivity.[3,4] Of the myriad redox-active motifs explored, the inclusion of heteroatoms with lone pairs strategically within a ligand framework is a particularly useful design principle for introducing reservoirs of electron-density accessible through ligand-based electron transfer. For example, redox-active biquinone *O^N^O* ligands have yielded transition metal complexes of unusual oxidation states,[5] often boasting impressive absorption profiles.[6] While these tridentate ligands contain central amido donors, their redox-active nature centres on the catecholate/semiquinonate couple. In the context of MCCs, nitrogen-based amido lone pairs can be oxidized to give metal-coordinated aminyl radicals and represent what is by now a common example of redox 'non-innocence'.[7] Metal-coordination of aminyl radicals has been exploited to access substrate-based radical-like reactivity[8,9] and interesting electronic/spectroscopic properties[10] derived from mixed-valence character, including strengthened absorption in the near IR (NIR).[11] Flanking aryl groups have a further stabilizing effect, and diarylamido architectures have been widely explored in this context.[12,13]

With respect to finding spectroscopic markers of ligand-based radicals in transition metal coordination complexes, the ability of MCCs of redox-active ligands to strongly absorb visible and NIR light can be beneficial.[14] Benzannulation is a common strategy for boosting the absorptive cross-sections of organic ligands and their coordination complexes.[15] We have investigated the incorporation of benzannulated phenanthridine (3,4-benzoquinoline) moieties in diarylamido ligands.[16] In addition to producing Pt MCCs that combine strong absorption and red-shifted phosphorescence,[17,18] neutral Fe-based MCCs comprised of two such ligands show strong panchromatic absorption and nanosecond charge-transfer lifetimes in their neutral forms, along with a rich redox profile.[19] Similarly strong but narrower absorption bands can also be seen with isoelectronic Co(III) analogues, as well as congeners of redox-silent Zn(II) and Ga(III) ions.[20] Together with a Ni(II) variant, this series presents a gradient of dπ–pπ mixing between filled metal d and amido N(2p) orbitals. Despite this gradient in orbital character, however, the redox chemistry of the MCCs based on metals other than iron is uniformly ligand-centred, with strong intervalence charge-transfer (IVCT) bands observed in the NIR upon oxidation (Fig. 1).

[a]*Department of Chemistry, University of Manitoba, 144 Dysart Road, Winnipeg, Manitoba, Canada. E-mail: david.herbert@umanitoba.ca*

[b]*Department of Physics and Astronomy, University of Manitoba, 31A Sifton Rd, Winnipeg, Manitoba, Canada*

[c]*Manitoba Institute for Materials, University of Manitoba, 20 Sifton Rd, Winnipeg, MB, Canada*

† Electronic supplementary information (ESI) available: Multi-nuclear NMR and HR-MS spectra; magnetism plots, DFT and TD-DFT tables and plots, and crystallographic information files containing all X-ray data. CCDC 2044311 and 2044312. For ESI and crystallographic data in CIF or other electronic format see DOI: 10.1039/d0ra10761a

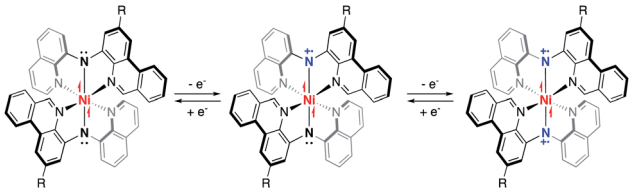

Fig. 1 Redox-related series of paramagnetic Ni(II) complexes of phenanthridine/quinoline containing diarylamido pincer-type ligands.

Compared with other common air-stable transition metal oxidation states, chromophores based on MCCs bearing d^8 Ni(II) ions outside of bis-dithiolenes[21] are relatively rare,[22,23] especially those displaying strong NIR absorptions.[24] In a notable example, a pseudo-octahedral Ni(II) complex of the non-innocent *N*,*N*′-bis(3,5-di-*tert*-butyl-2-hydroxy-phenyl)-1,2-phenylenediamine ligand was recently shown to exhibit very strong absorptive cross-sections well into the NIR[25] thanks to the redox-active nature of the ligand. Noting the strengthened absorptive properties enabled by our readily synthesized benzannulated diarylamido ligands, we report here a series of three pseudo-octahedral nickel complexes of phenanthridine/quinoline-based diarlyamido ligands and describe the impact that ligand substitution has on their electronic structures and stabilities upon oxidation. We find that a degree of covalency to the Ni–N_{amido} interaction strengthens the IVCT features observed. This work is meant to contribute examples of strongly absorbing MCCs to the growing literature describing electronic communication between organic fragments mediated by metal bridges.[26,27]

Results and discussion

Compared with quinoline and acridine, the coordination chemistry of phenanthridine-containing multidentate ligand scaffolds is much less developed.[28] We previously described the preparation of (4-amino)phenanthridines amenable for incorporation into multidentate ligands, including those bearing methyl,[16] *tert*-butyl (*t*Bu; **1a**)[19] and trifluoromethyl (**1b**)[29] substituents in the 2-position of the heterocycle. Here, we extend this methodology to include installation of a halide (Cl; **1c**). Briefly, tandem Suzuki coupling/condensation reaction of 2-formylphenyl boronic acid and (2-iodo-6-nitro-4-chloro) aniline affords **1c** in 65% yield (Scheme 1a). Reduction of (4-nitro-2-chloro)phenanthridine **1c** to (4-amino-2-chloro) phenanthridine **1e** was accomplished in a facile manner using zinc and a hydrazine/formate mixture (analogous to the preparation of **1d**[19]). Pd-catalyzed C–N coupling of **1e** with commercially available (8-bromo)quinoline gave the desired proligand ^{Cl}**LH** in 90% isolated yield. The preparation of all three proligands ^{R}**LH** is summarized in Scheme 1b. Metalation with Ni(II) was achieved in refluxing methanol using $NiCl_2 \cdot 6H_2O$ and an exogenous base in the same manner as reported for $(^{tBu}\mathbf{L})_2$Ni.[20]

The resulting complexes are deep red. All are paramagnetic and in solution present broad ^{1}H NMR spectra covering an

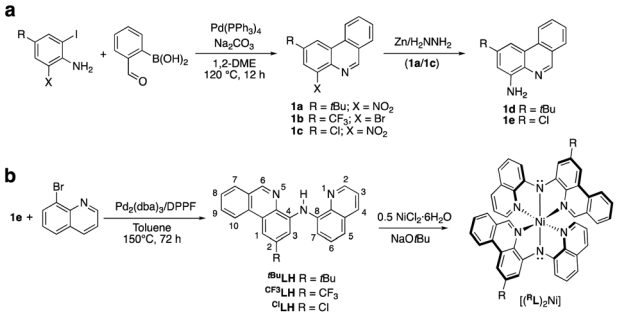

Scheme 1 Synthesis of (a) **1a–e**; and (b) proligands ^{R}LH and their $(^{R}L)_2$Ni complexes. See noted references for conditions for preparation of **1a**, **1b**, **1d**, ^{tBu}LH, ^{CF3}LH and $(^{tBu}L)_2$Ni. The IUPAC numbering system for quinolines and phenanthridines is illustrated for ^{R}LH.

expanded chemical shift range of 0–45 ppm (Fig. S1 and S2†). Evans' method NMR experiments (Fig. S3 and S4†) are consistent with two unpaired electrons [$\mu_{eff} = 2.90\ \mu_B$ (^{tBu}**L**)$_2$Ni,[20] 2.68 μ_B (^{CF3}**L**)$_2$Ni, 2.97 μ_B (^{Cl}**L**)$_2$Ni]. Solid-state SQUID magnetometry agrees with this assignment [$\mu_{eff} = 2.99(3)\ \mu_B$ (^{tBu}**L**)$_2$Ni, 3.02(3) μ_B (^{CF3}**L**)$_2$Ni, 2.82(3) μ_B (^{Cl}**L**)$_2$Ni; Fig. S5–S7†]. The molecular formulae of the 20-electron complexes were corroborated by high-resolution mass spectrometry (HR-MS). For the new complexes, (^{CF3}**L**)$_2$Ni and (^{Cl}**L**)$_2$Ni, crystals suitable for X-ray diffraction were obtained by slow evaporation of pentane solutions. The solid-state structures show the metal in a pseudo-octahedral coordination environment with two N_{amido} donors *trans* to each other (Fig. 2; see Table S1† for a summary of bond distances and angles). As expected, the shortest Ni–N contacts involve the anionic N_{amido} nitrogens and are very similar among the three complexes ranging from 2.00–2.02 Å. Contacts between the metal and the *N*-heterocyclic N donor atoms are also very similar, spanning only a narrow range from 2.06–2.09 Å. In comparison, the 18-electron d^6 analogue (^{tBu}**L**)$_2$Fe exhibits

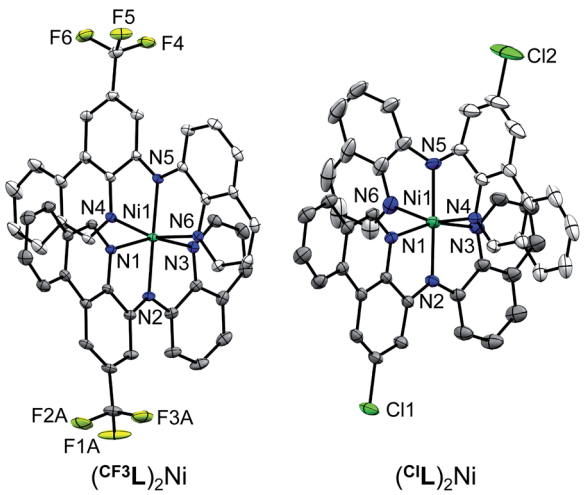

Fig. 2 Solid-state structures of (^{CF3}L)$_2$Ni and (^{Cl}L)$_2$Ni with thermal ellipsoids shown at 30% probability levels. Carbon atom labels, hydrogen atoms, disordered component to one CF_3 group and co-crystallized solvent molecules have been omitted for clarity.

a tighter coordination environment with M–N_{amido} bond lengths of ~1.90 Å and M–$N_{phen/quin}$ bond lengths of ~1.90–1.97 Å,[19] correlating with trends in ionic radii.[30]

The electronic structure of the Ni complexes was probed by electrochemical techniques using cyclic voltammetry (CV) and differential pulse voltammetry (DPV; Fig. 3). The precise onset of the broad, irreversible reduction events for the complexes is difficult to assign, but the observation of cathodic events past ~−2.5 V *vs.* ferrocene/ferrocenium ($FcH^{0/+}$) is consistent with ligand-based reduction, specifically at the phenanthridinyl arm.[19] The oxidative chemistry of all three complexes is also similar within the series, though the identity of the substituent in the 2-position has a notable influence on both the potential and reversibility of the oxidation. These two effects do not trend together, however, as the oxidation events for $(^{Cl}L)_2Ni$ are the least reversible, though not the most anodically shifted (Table 1). As befits the electronic influence of the three substituents, the oxidation potentials shift to more positive values as the substitution on the ligand changes from electron-releasing (*t*Bu, $E_{ox1} = -0.23$ V *vs.* $FcH^{0/+}$) to increasingly electron-withdrawing (Cl, $E_{ox1} = -0.19$ V *vs.* $FcH^{0/+}$; CF_3, $E_{ox1} = -0.05$ V *vs.* $FcH^{0/+}$) in accordance with their respective *meta* Hammett substituent constants[31] (*t*Bu = −0.10; Cl = +0.37; CF_3 = +0.43). These anodic events are consistent with the formation of aminyl radical character at the N_{amido} nitrogen atoms, stabilized to some degree by ligation to the metal.[12]

Electronic absorption spectra of the complexes in CH_3CN solution are shown in Fig. 4. The deep red complexes absorb strongly peaking near 500 nm (ε = ~30 000 M^{-1} cm^{-1}), with marked shifts as a function of ligand substitution. The lowest-energy peak of $(^{tBu}L)_2Ni$ is the most red-shifted (Table 1), with the electron-releasing *t*Bu group destabilizing the HOMO through electronic effects. In comparison, the lowest energy absorptions of $(^{CF3}L)_2Ni$ and $(^{Cl}L)_2Ni$ are present at slightly higher energy. For these latter complexes, unlike the oxidation potential, the peak position and band edge does not track exactly with the electron-withdrawing character derived from Hammett substituent constants;[31] the λ_{max} for $(^{Cl}L)_2Ni$ is more blue-shifted than that of $(^{CF3}L)_2Ni$. The overall effect is inverted from what is seen for $(^{R}L)_2Fe$ (R = CF_3, *t*Bu).[19] Time-dependent DFT (TDDFT) reveals subtle functional group effects. Exchanging an electron-releasing (R = *t*Bu) substituent for an electron withdrawing one (R = CF_3, Cl), a decrease in the number of electronic excitations (f_{osc} > 0.05) are observed within the lowest energy absorption band (E < 2.8 eV; *t*Bu = 6,[20] CF_3 = 5; Cl = 4). Furthermore, configuration interactions of multiple contributing (>10%) particle-hole pairs in a given state decrease when electron-withdrawing substituents are present. These effects seem to be the origin of the discrepancy between the experimental λ_{max} of $(^{Cl}L)_2Ni$ and $(^{CF3}L)_2Ni$, and their respective Hammett substituent constants. Compared with the d^8 complexes investigated here, the phenanthridine substituent most strongly influences the LUMO energy in d^6 Fe(II) complexes and $(^{CF3}L)_2Fe$ (bearing the more strongly electron-withdrawing substituent on the heterocycle) absorbs to lower energy than $(^{tBu}L)_2Fe$.

Density functional theory (DFT) optimization of $(^{CF3}L)_2Ni$ and $(^{Cl}L)_2Ni$ reproduced the structural metrics observed in the solid-state using the same basis set and method reported for $(^{tBu}L)_2Ni$[20] (Table S2;† SMD-O3LYP/6-31+G(d,p)). Consistent with the observed trends in the Ni–N distances in the solid-state, DFT predicts shorter Ni–N_{amido} distances compared to the Ni–N_{phen}/Ni–N_{quin} separations, with minimal differences between the Ni–N_{phen} and Ni–N_{quin} values. The electronic

Table 1 Redox potentials (V) and absorbance parameters for Ni complexes, λ (nm), ε in parenthesis (M^{-1} cm^{-1})

Compound	$[(^{tBu}L)_2Ni]^{0/1+/2+}$	$[(^{CF3}L)_2Ni]^{0/1+/2+}$	$[(^{Cl}L)_2Ni]^{0/1+/2+}$
E_{ox1} [a]	−0.23	−0.05	−0.19
E_{ox2} [a]	−0.04	+0.15	+0.11
ΔE_1° [b]	0.19	0.20	0.30
λ_{max} $(^{R}L)_2Ni$	519 (28 370)	508 (28 890)	503 (27 170)
λ_{max} $[(^{R}L)_2Ni]^+$	1802 (15 740)	1729 (14 400)	1751 (4970)
λ_{max} $[(^{R}L)_2Ni]^{2+}$	683 (101 430)	663 (59 170)	689 (19 030)

[a] Oxidation potentials starting from $(^{R}L)_2Ni$ *vs.* $Fc/FcH^{0/+}$. [b] $E_{ox2} - E_{ox1}$.

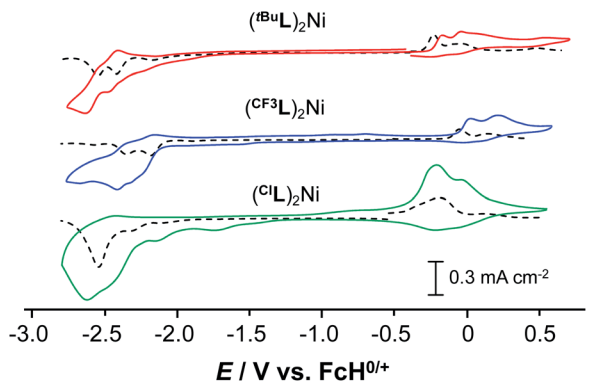

Fig. 3 Cyclic voltammograms (—) and differential pulse voltammograms (—) of $(^{R}L)_2Ni$ in CH_3CN with 0.10 M $[nBu_4N][PF_6]$ as the supporting electrolyte, using a glassy carbon working electrode. CV scan rates were 100 mV s^{-1}. Potentials are listed *vs.* the $FcH^{0/+}$ redox couple (FcH = ferrocene).

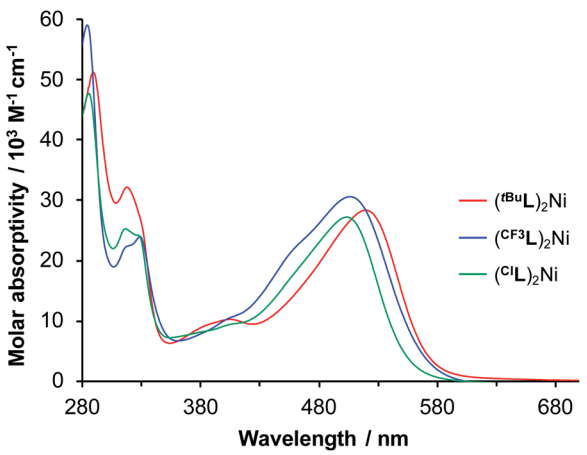

Fig. 4 UV-vis absorption spectra of $(^{R}L)_2Ni$ in CH_3CN.

structures optimized in the triplet spin-state corroborate the Evans' method and solid-state magnetometry results. For both $(^{CF3}L)_2Ni$ and $(^{Cl}L)_2Ni$, spin density plots show localization of the unpaired electrons at the metal (Fig. S8†). Accordingly, the two singly occupied molecular orbitals (SOMOs) are predicted by DFT to be metal-based, primarily of d_{z^2} and $d_{x^2-y^2}$ character, with fragment contributions to the respective orbitals by Ni of 80% and 84%, respectively (Table S3†), as befits a pseudo-octahedral ligand field and a d^8 Ni(II) ion.[32]

An orbital energy level diagram showing the two SOMOs, the next three highest energy fully occupied MOs, and the lowest unoccupied molecular orbitals (LUMOs) of $(^{CF3}L)_2Ni$ is shown in Fig. 5. The LUMO and LUMO+1 are both low-lying ligand-based π* orbitals with significant contributions from the (H)C=N_{phen} subunit of the phenanthridinyl arm of the benzannulated ligand framework (26% for the LUMO; see Table S3† for population analysis). Thus, ^{R}L retains its strong electron-accepting character. In related Ni(II) complexes of pyrazolyl diarylamido ligands[27] the metal centre was described as an isolated Ni(II) ion sitting within an N_6 coordination environment, only interacting weakly with filled ligand π-type orbitals. While the filled–filled interactions between the metal dπ and amido pπ-type orbitals is not as strong as for the analogous Fe(II) complexes[19] there a non-negligible contribution to the SOMO from the N_{amido} units, and metal participation in the next highest-lying filled MOs (labelled $n_{N,am}\pi$ in Fig. 5; see Table S3† for population analysis). Electron-withdrawing substituents (R = CF_3, Cl) on the phenanthridinyl arms stabilize the energy of the N_{amido} orbitals relative to the electron releasing *t*Bu-substituent but their characters are unperturbed, again evident from the population analysis. These are consistent with the experimental redox potentials (Table 1) and assigned aminyl radical character.

The MCCs were next characterized using spectroelectrochemistry to ascertain the spectroscopic response to oxidation. Upon single-electron oxidation (Fig. 6a, c and e), the lowest energy absorption band for each of $(^{R}L)_2Ni$ at ~500 nm attenuates rapidly, with the growth of a new peak at ~700 nm and a considerably broader, lower energy NIR absorption at ~1800 nm (FWHM ~ 3000 cm^{-1}), typical of oxidized metal-bridged diarylamines.[33] The strong absorptivity values (ε = ~16 000 M^{-1} cm^{-1} for $[(^{tBu}L)_2Ni]^+$ and $[(^{CF3}L)_2Ni]^+$, ~5000 M^{-1} cm^{-1} for $[(^{Cl}L)_2Ni]^+$) and position of this new absorption are consistent with an intervalence charge-transfer (IVCT) transition from one N_{amido} lone pair to the aminyl radical on the opposing ligand, mediated through the Ni metal centre.[11] A structurally distinct square-planar Ni(II) dye with a similarly intense but narrower absorption at ~1000 nm has been described.[24] That complex also contained a ligand-based radical, localized on a 3,5-(dimedonyl)azadiisoindomethene scaffold. For that system, reduction of the paramagnetic complex to a neutral anion brought about the appearance of an even stronger absorption at 748 nm and disappearance of the NIR absorption at 1008 nm. The NIR peaks attenuated upon oxidation. Here, the second oxidation of $(^{R}L)_2Ni$ to $[(^{R}L)_2Ni]^{2+}$ results in the disappearance of the low-energy peak but continued growth of the strong peak at ~700 nm (Fig. 6b, d and f). This is consistent with two completely oxidized N_{amido} fragments, and a blue colour could be seen in the spectroelectrochemical cell. Compared with $(^{tBu}L)_2Ni$ and $(^{CF3}L)_2Ni$, $(^{Cl}L)_2Ni$ initially appears to follow the same trend, however, each new peak observed is much smaller in intensity. Also,

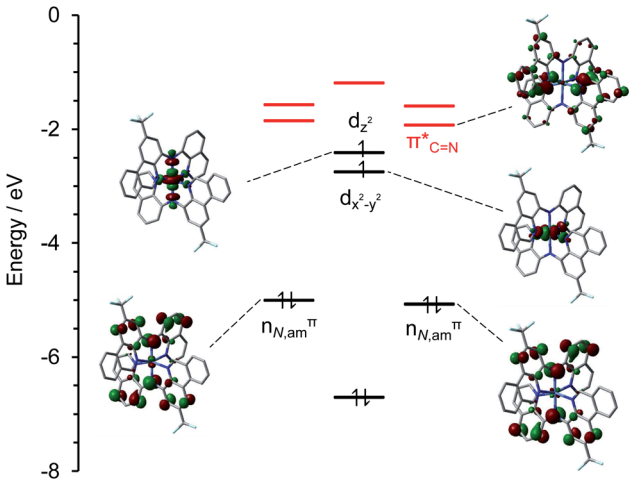

Fig. 5 Selected ground-state restricted open-shell molecular orbital isosurfaces (isovalue = 0.04) and energy diagram for $(^{CF3}L)_2Ni$ (SMD-roPBE0/6-31+G(d,p)//SMD-uO3LYP/6-31+G(d,p)). Vacant, acceptor ligand-based π* orbitals are highlighted in red. Fragment contributions to selected MOs are tabulated in Table S3.†

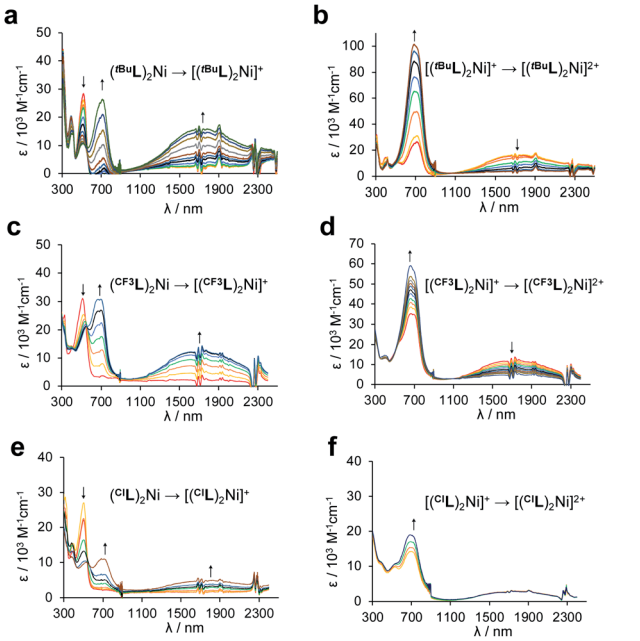

Fig. 6 UV-Vis/NIR absorption spectra 0.3 M $[nBu_4N][PF_6]$ CH_3CN solution of (a) $(^{tBu}L)_2Ni$, oxidative potentials applied from −0.1 to 0.35 V; (b) $(^{tBu}L)_2Ni$, oxidative potentials applied from 0.35 to 1.4 V; (c) $(^{CF3}L)_2Ni$, oxidative potentials applied from −0.3 to 0.8 V; (d) $(^{CF3}L)_2Ni$, oxidative potentials applied from 0.8 to 1.4 V; (e) $(^{Cl}L)_2Ni$, oxidative potentials applied from −0.1 to 0.7 V; and (f) $(^{Cl}L)_2Ni$, oxidative potentials applied from 0.7 to 1.3 V. All potentials referenced to Ag/Ag^+.

particulate matter could be observed deposited in the cell following the experiment. The degradation of $(^{Cl}L)_2Ni$ upon oxidation is the likely cause of the difference in peak intensity and corroborates the electrochemical irreversibility seen in the CV of $(^{Cl}L)_2Ni$ compared to $(^{tBu}L)_2Ni$ and $(^{CF3}L)_2Ni$.

The electrochemical and spectroelectrochemical data together reveal a degree of metal-mediated electronic communication between the N_{amido} fragments in the three complexes. Observation of a second separated, though irreversible, oxidation in the CV, and the presence of IVCT bands, support this claim and negate the competing possibility of coulombic effects.[27] Similar observations have recently been made of Ni complexes supported by sterically hindered salen ligands,[34] and more comparably, for pseudo-octahedral Ga(III) complexes of di(2-3*R*-pyrazolyl)-*p*-arylamine ligands.[26] Upon exchanging Ga(III) for Ni(II) in that ligand environment, the electronic communication is significantly enhanced owing to strengthened (although still relatively weak) dπ–pπ interactions between Ni d orbitals and amido p orbitals.[27] A similar degree of mixing appears to operate in $[(^{R}L)_2Ni]^{0/1+/2+}$, with strong IVCT features observed for $[(^{R}L)_2Ni]^{+}$.

Accordingly, quantitative analysis of the electronic relationship between the electroactive N_{amido} centres can be carried out using classical Marcus[35] theory along with Hush[36] relations (Table 2; see equations in ESI†). Comproportionation constants (K_{com}) gleaned from the electrochemical data suggest that all three complexes exhibit Robin-Day Class II behavior.[37] Spectroelectrochemical data supports a Class IIB assignment for $(^{CF3}L)_2Ni$ (H_{ab} = 2432 cm^{-1}), very similar to that reported for $(^{tBu}L)_2Ni$ (Table 2).[20] Though $(^{Cl}L)_2Ni$ has a larger K_{com} value (1.33×10^5) than $(^{tBu}L)_2Ni$ or $(^{CF3}L)_2Ni$, likely due to exhibiting the most irreversible oxidations, IVCT analysis suggests electronic communication in the Robin-Day Class IIA regime (H_{ab} = 1703 cm^{-1}; Table 2). However, in light of the aforementioned decomposition of $(^{Cl}L)_2Ni$ under conditions of spectroelectrochemical analysis, Class IIB assignment may be more appropriate. Comparing these complexes to the homoleptic Ga and Ni complexes of pyrazolyl diarlyamido ligands mentioned above,[26,27] ε values nearing 20 times greater are observed in the NIR region of the absorption spectra.

The MO diagram, spin-density maps and magnetism are all consistent with a paramagnetic d^8 Ni(II) ion in an octahedral ligand field. Yet, the spectroelectrochemical response suggests formation of a ligand-based radical, supported by the covalency implied by the strong IVCT features for the oxidized species. Similar non-Aufbau behaviour has been reported for vanadium porphyrinate and phthalocyanines,[38] as well as for closely related pseudo-octahedral Ni complexes,[27] where the minimization of the spin-pairing energy favours removal of an electron from a lower-lying N_{amido} lone-pair orbital rather than from a higher energy metal-based SOMO. Accordingly, time-dependent DFT (TDDFT) simulations (Fig. S9–S12†) identify three to five electronic transitions with significant oscillator strengths ($f_{osc} > 0.05$; Tables S6 and S7†) in the lowest energy band ($E < 3$ eV) of the experimental UV-vis spectra as ligand-to-ligand charge-transfer (LLCT) from the N_{amido} lone pair to the LUMO, rather than involving the metal-based SOMOs, further supporting the non-Aufbau assignment. In all cases, the acceptor orbital (LUMO) is mainly localized on the phenanthridine imine-like C=N unit.

Table 2 Summary of IVCT band analysis for electrochemically generated $[(^{R}L)_2Ni]^{+}$

Compound	$[(^{tBu}L)_2Ni]^{+}$	$[(^{CF3}L)_2Ni]^{+}$	$[(^{Cl}L)_2Ni]^{+}$
$E_{OP} = \lambda$ (cm^{-1})	5549	5784	5711
ε_{max} (M^{-1} cm^{-1})	15 740	14 400	4970[a]
$\Delta\nu_{1/2}$ (cm^{-1})	3051	2781	3998
$\Delta\nu_{1/2}$ HTL (cm^{-1})	3580	3627	3604
$\theta = \Delta\nu_{1/2}/\Delta\nu_{1/2}$ (HTL)	0.852	0.767	1.109
d (Å)[b]	4.055[c]	4.055[c]	4.055[c]
H_{ab} (cm^{-1})	2609	2432	1703
$\alpha = 2H_{ab}/\lambda$	0.940	0.841	0.596
ΔG^* (cm^{-1})	4.936	36.58	232.6
k_{et} (s^{-1})	2.065×10^{15}	1.505×10^{15}	2.859×10^{14}
K_{com}[d]	1.76×10^3	2.61×10^3	1.33×10^5
	Class IIB	Class IIB	Class IIB[a]

[a] Value for extinction coefficient may be artificially low due to decomposition. See text for full discussion of implications for Class IIB *vs.* IIA assignment. [b] Distance (Å) between electroactive N_{amido} centres. [c] Average value from DFT-optimized structure of $[(^{tBu}L)_2Ni]^{+}$ [S = 3/2; SMD-uPBE0/6-31+G(d,p)]. Due to the similarities of the other complexes to $[(^{tBu}L)_2Ni]^{+}$, DFT was not run for these complexes. Note: very small differences were observed between calculated bond distances of $[(^{tBu}L)_2Ni]$ and $[(^{tBu}L)_2Ni]^{+}$. [d] $K_{com} = e^{(\Delta EF/RT)}$, T = 295 K; $k_B = 0.695$ cm^{-1} K^{-1}; $h = 3.36 \times 10^{-11}$ cm^{-1} s; T = 295 K.

Conclusions

The use of a benzannulated *N*^*N*^*N* tridentate diarylamido ligand has afforded deeply coloured pseudo-octahedral d^8 Ni complexes that exhibit non-Aufbau behaviour in their electronic structures. Introducing highly energetic N_{amido}-based lone pairs into the frontier orbital manifold gives rise to several ligand-derived transitions with significantly large epsilon values, ascribable to the extended π system offered by the phenanthridine/quinoline donors.

Incorporating the synthetically tunable phenanthridine moiety into this ligand scaffold furthermore allowed us to study the impact of ligand substitution on the electrochemical and absorptive properties of these complexes and their oxidized analogues. We find that although the electronic properties of the neutral complexes are quite similar, they differ upon oxidation in terms of oxidative potential and the stability of the radical species evidenced by spectroelectrochemical data. The exceptionally strong IVCT bands observed in $(^{tBu}L)_2Ni$ and $(^{CF3}L)_2Ni$ are on the order of 20× more intense than previous examples of electronic communication of oxidized diarylamido N(2p) lone pairs across paramagnetic Ni bridges[27] in an octahedral geometry, revealing the impact of the benzannulated ligand framework.

Experimental

Materials

Unless otherwise specified, air-sensitive manipulations were carried either in a N_2 filled glove box or using standard Schlenk techniques under Ar. 2-Formylphenyl boronic acid, *N*-

iodosuccinimide (AK Scientific); $Pd(PPh_3)_4$; $Pd_2(dba)_3$, (1,1′-diphenylphosphino)ferrocene (dppf), sodium *tert*-butoxide (NaO*t*Bu), hydrazine hydrate (Sigma Aldrich), 4-chloro-2-nitronaniline (Combi-Blocks), Na_2CO_3, zinc, formic acid, and $NiCl_2 \cdot 6H_2O$ (Alfa Aesar) were used as purchased.

Organic solvents were dried and distilled using appropriate drying agents prior to use. 1- and 2D NMR spectra were recorded on Bruker Avance 300 MHz or Bruker Avance – III 500 MHz spectrometers. ^{1}H and $^{13}C\{^1H\}$ NMR spectra were referenced to residual solvent peaks. Elemental analyses were performed at the University of Manitoba using a PerkinElmer 2400 Series II CHNS/O Elemental Analyzer. ^{tBu}**LH** and ^{CF3}**LH** were synthesized according to literature procedures.[19]

Instrumentation and methods

For electrochemical analysis, 5–10 mg of each compound investigated was dissolved in 15 mL of 0.1 M [nBu$_4$N][PF$_6$] in CH_3CN and purged with Ar for 20 minutes before analysis. All electrochemical experiments were conducted under inert (Ar) atmosphere using a CHI 760c bipotentiostat, a 3 mm diameter glassy carbon working electrode, a Ag/Ag^+ quasi-non-aqueous reference electrode separated by a Vycor tip, and a Pt wire counter electrode. Cyclic voltammetry (CV) experiments were conducted using scan rates of 50–800 mV s^{-1}. Differential pulse voltammetry (DPV) experiments were also conducted, using a 5 mV increment, 50 mV amplitude, 0.1 s pulse width, 0.0167 s sample width, and 0.5 s pulse period. Upon completion of all CV and DPV analyses, ferrocene (FcH) was added to the solution as an internal standard, with all potentials reported *versus* the $FcH^{0/+}$ redox couple. Magnetic measurements were performed using a Quantum Design MPMS-XL SQUID magnetometer. Samples were mounted in NMR Suprasil quartz tubes. Susceptibility was measured on cooling from 300–2 K, in an applied field of 0.1 T. After reaching 2 K, magnetization measurements were performed from 0–5 T. Magnetic moments (μ_{eff}) were obtained by fitting $1/\chi$ using a modified Curie–Weiss law, with a subtraction performed on χ accounting for the diamagnetic components arising from the ligands using Pascal's method.[39]

Synthesis

2-Iodo-6-nitro-4-chloroaniline. A 500 mL round-bottom flask was charged with 4-chloro-2-nitroaniline (10.0 g, 0.058 mol), *N*-iodosuccinimide (13.7 g, 0.061 mol) and acetic acid (200 mL). The mixture was heated to 60 °C for 72 h and then poured over ice. The mixture was then filtered, and the precipitate dissolved in dichloromethane (100 mL) then washed with water (3 × 100 mL). The solvent was then removed to leave an orange solid. Isolated yield = 15.3 g (88%). The ^{1}H NMR spectrum of the isolated product contained ~10% starting material, however, the compound could be used without further purification. The NMR matches the literature.[40]

4-Nitro-2-chlorophenanthridine (1c). A 350 mL Teflon-stoppered flask was charged with $Pd(PPh_3)_4$ (0.39 g, 1.54 mmol) and 50 mL of DME. After stirring briefly to mix, 2-iodo-6-nitro-4-chloroaniline (15.3 g, 0.34 mmol), 2-formylphenylboronic acid (1.11 g, 7.37 mmol) and an additional 70 mL of DME were added, followed by Na_2CO_3 (2.13 g, 2.0 mmol) dissolved in 100 mL of degassed water. The flask was sealed, and the mixture stirred vigorously for 6 h in an oil bath (130 °C). The mixture was then pumped to dryness. The residue was then taken up in dichloromethane (100 mL) and filtered followed by washings with brine (3 × 100 mL). The organic layer was separated, dried over Na_2SO_4 and volatiles removed. Removal of triphenylphosphine oxide was accomplished by heating the mixture in toluene and adding excess $MgCl_2$ and stirring overnight. Filtration and removal of solvent left a yellow-brown solid. Isolated yield = 1.12 g (65%). ^{1}H NMR ($CDCl_3$, 300 MHz, 25 °C): δ 9.37 (s, 1H, $C_{Ar}H$), 8.70 (d, 1H, J_{HH} = 2.2 Hz, $C_{Ar}H$), 8.55 (dd, 1H, J_{HH} = 8.4, 1.0 Hz, $C_{Ar}H$), 8.18–8.12 (overlapped m, 1H, $C_{Ar}H$), 8.04–7.94 (m, 1H, $C_{Ar}H$), 7.95 (d, 1H, J_{HH} = 2.2 Hz; $C_{Ar}H$), 7.87 ppm (ddd, J_{HH} = 8.1, 7.2, 1.1 Hz 1H, $C_{Ar}H$). $^{13}C\{^1H\}$ NMR ($CDCl_3$, 75 MHz, 25 °C): δ 156.1 (C_{Ar}), 149.7 (C_{Ar}), 134.5 (C_{Ar}), 132.6 (C_{Ar}), 132.3 (C_{Ar}), 132.1 (C_{Ar}), 130.5 (C_{Ar}), 129.7 (C_{Ar}), 129.5 (C_{Ar}), 126.8 (C_{Ar}), 125.4 (C_{Ar}), 122.9 (C_{Ar}), 122.3 ppm (C_{Ar}).

4-Amino-2-chlorophenanthridine (1e). To a stirred solution of 4-nitro-2-chlorophenanthridine (12.0 g, 46.4 mmol) in methanol (200 mL), Zn dust (6.1 g, 92.8 mmol), and hydrazinium monoformate solution (119.3 mL; prepared by slowly neutralizing equal molar amounts of hydrazine hydrate (110 mL) with 85% formic acid (9.3 mL) in an ice-water bath) were added and stirred vigorously at 60 °C overnight. The resulting green suspension was cooled and filtered over Celite. The filtrate was pumped dry, the residue dissolved in dichloromethane (100 mL), and washed with brine (3 × 60 mL). The organic layer was separated, dried over Na_2SO_4 and dried to leave a green-brown solid, which was purified by running a dichloromethane solution over silica. Isolated yield = 9.32 g (88%). ^{1}H NMR ($CDCl_3$, 300 MHz, 25 °C): δ 9.07 (s, 1H, $C_{Ar}H$), 8.42 (dd, 1H, J_{HH} = 8.2 Hz; $C_{Ar}H$), 8.00 (dd, 1H, J_{HH} = 8.0, 1.4 Hz; $C_{Ar}H$), 7.79 (m, 2H, $C_{Ar}H$), 7.69 (ddd, 1H, J_{HH} = 8.1, 7.0, 1.2 Hz; $C_{Ar}H$), 6.94 (d, 1H, J_{HH} = 2.1 Hz; $C_{Ar}H$), 5.14 ppm (s, 2H, NH_2). $^{13}C\{^1H\}$ NMR ($CDCl_3$, 75 MHz, 25 °C): δ 150.3 (C_{Ar}), 146.0 (C_{Ar}), 133.8 (C_{Ar}), 132.0 (C_{Ar}), 131.9 (C_{Ar}), 131.0 (C_{Ar}), 128.7 (C_{Ar}), 127.9 (C_{Ar}), 127.0 (C_{Ar}), 125.7 (C_{Ar}), 122.5 (C_{Ar}), 111.2 (C_{Ar}), 110.2 ppm (C_{Ar}).

^{Cl}**LH.** A 500 mL Teflon-stoppered flask was charged with $Pd_2(dba)_3$ (0.12 g, 0.13 mmol), dppf (0.17 g, 0.31 mmol) and toluene (30 mL). After stirring for 5 minutes, 8-bromoquinoline (0.91 g, 4.37 mmol), 4-amino-2-chlorophenanthridine (1.0 g, 4.37 mmol), and an additional 20 mL of toluene were added, followed by sodium *tert*-butoxide (NaO*t*Bu; 0.63 g, 6.56 mmol). The reaction mixture was stirred and subjected to reflux in an oil bath set at 150 °C for 72 h. After cooling the flask, the volatiles were removed, and the residue was taken up in dichloromethane. The suspension was then filtered over a silica plug and the solvent was removed to leave a brown solid. Isolated yield = 1.40 g (90%). ^{1}H NMR ($CDCl_3$, 500 MHz, 25 °C): δ 10.75 (s, 1H, N–H), 9.27 (s, 1H, C_1–H), 8.97 (dd, 1H, J_{HH} = 4.2, 1.7 Hz, C_{14}–H), 8.46 (d, 1H, J_{HH} = 8.2 Hz, C_3–H), 8.15 (dd, 1H, J_{HH} = 8.3, 1.7 Hz, C_{16}–H), 8.05 (m, 1H, C_6–H), 7.95 (d, 1H, J_{HH} = 2.1 Hz, C_{13}–H), 7.96–7.83 (m, 2H, C_{11}–H, C_{22}–H), 7.82 (ddd, 1H, J_{HH} = 8.0, 7.1, 1.1 Hz C_5–H), 7.70 (ddd, 1H, J_{HH} = 8.0, 7.0, 1.1 Hz

C_4–H), 7.55 (t, 1H, J_{HH} = 8.0 Hz, C_{21}–H), 7.47 (dd, 1H, J_{HH} = 8.3, 4.2 Hz, C_{15}–H), 7.37 ppm (dd, 1H, J_{HH} = 8.2, 1.2 Hz, C_{20}–H). $^{13}C\{^1H\}$ NMR ($CDCl_3$, 125 MHz, 25 °C): 150.9 (C_1), 148.4 (C_{14}), 140.8 (C_{10}), 140.2 (C_{19}), 138.2 ($C_{17\ or\ 18}$), 136.3 (C_{16}), 133.9 ($C_{17\ or\ 18}$), 133.6 ($C_{8\ or\ 9}$), 132.0 ($C_{2\ or\ 7}$), 131.1 (C_5), 129.1 ($C_{8\ or\ 9}$), 128.9 (C_6), 128.0 (C_4), 127.2 (C_{21}), 127.1 ($C_{2\ or\ 7}$), 125.7 (C_{12}), 122.5 (C_3), 121.8 (C_{15}), 118.8 (C_{20}), 111.8 (C_{13}), 110.9 ($C_{11\ or\ C22}$), 110.7 (C_{11} or C_{22}).

(^{CF3}L)$_2$Ni. A 100 mL Teflon-stoppered flask was charged with $NiCl_2 \cdot 6H_2O$ (0.030 g, 0.13 mmol), **^{CF3}LH** (0.100 g, 0.26 mmol), and NaO*t*Bu (0.025 g, 0.26 mmol). Methanol (10 mL) was added and the flask was stirred and refluxed at 100 °C overnight. The flask was then cooled to room temperature and stirred for 1 h. The solvent was then removed, and the red compound was dissolved again in minimal CH_2Cl_2 (5 mL) and filtered over Celite. The solvent was then removed leaving a bright red solid. Isolated yield = 0.105 g (>99%). ^{1}H NMR ($CDCl_3$, 300 MHz): δ 44.5 (br), 33.0 (br), 30.9 (br), 19.7 (br), 17.4 (br), 13.2 (s), 12.3 (br), 10.4 (s), 5.5 ppm (s). UV-vis (CH_3CN): λ (ε) 284 (59 040), 317 (22 310), 329 (24 010), 407 (sh), 455 (sh), 508 nm (28 890 M^{-1} cm^{-1}). μ_{eff} (Evans' method) = 2.68 μ_B. MS (ESI-TOF/MS, *m*/*z*) calcd for $C_{46}H_{26}F_6N_6Ni$ $[M]^+$, 834.1471; found 834.1482.

(^{Cl}L)$_2$Ni. A 100 mL Teflon-stoppered flask was charged with $NiCl_2 \cdot 6H_2O$ (0.033 g, 0.14 mmol), **^{Cl}LH** (0.1 g, 0.28 mmol), and NaO*t*Bu (0.027 g, 0.28 mmol). Methanol (10 mL) was added and the flask was stirred and refluxed at 100 °C overnight. The flask was then cooled to room temperature and stirred for 1 h. The solvent was then removed, and the red compound was dissolved again in minimal CH_2Cl_2 (5 mL) and filtered over Celite. The solvent was then removed leaving a bright red solid. Isolated yield = 0.105 g (>99%). ^{1}H NMR ($CDCl_3$, 300 MHz): δ 44.3 (br), 33.0 (br), 27.3 (br), 19.8 (br), 17.4 (br), 13.2 (s), 12.1 (br), 10.5 (s), 5.3 (br). UV-vis (CH_3CN): λ (ε) 286 (47 600), 316 (25 220), 406 (sh), 503 nm (27 170 M^{-1} cm^{-1}). μ_{eff} (Evans' method) = 2.97 μ_B. MS (ESI-TOF/MS, *m*/*z*) calcd for $C_{44}H_{26}Cl_2N_6Ni$ $[M]^+$, 766.0944; found 766.0963.

X-ray crystallography

X-ray crystal structure data was collected in each case from a multi-faceted crystal of suitable size and quality selected from a representative sample of crystals of the same habit using an optical microscope. The crystals were mounted on MiTiGen loops and data collection carried out in a cold stream of nitrogen (150 K; Bruker D8 QUEST ECO; Mo K_α radiation). All diffractometer manipulations were carried out using Bruker APEX3 software.[41] Structure solution and refinement was carried out using XS, XT and XL software, embedded within Olex2.[42] For each structure, the absence of additional symmetry was confirmed using ADDSYM incorporated in the PLATON program.[43]

Crystal structure data for (^{CF3}L)$_2$Ni (CCDC 2044311†). Crystals were grown by slow evaporation of a pentane solution. Red blocks; $C_{56}H_{50}F_6N_6Ni$ 979.73 g mol^{-1}, monoclinic, space group $P\bar{1}$; a = 11.9342(6) Å, b = 14.6616(7) Å, c = 16.6289(8) Å, α = 113.683(2)°, β = 90.763(2)°, γ = 113.819(2)°, V = 2383.5(2) $Å^3$; Z = 2, ρ_{calcd} = 1.365 g cm^{-3}; crystal dimensions 0.270 × 0.150 × 0.110 mm; $2\theta_{max}$ = 55.058°; 68 060 reflections, 10 937 independent (R_{int} = 0.0580), intrinsic phasing; absorption coeff (μ = 0.476 mm^{-1}), absorption correction semi-empirical from equivalents (SADABS); refinement (against F_o^2) with SHELXTL V6.1, 654 parameters, 0 restraints, R_1 = 0.0511 ($I > 2\sigma$) and wR_2 = 0.1191 (all data), Goof = 1.046, residual electron density 0.72/−0.66 $Å^{-3}$.

Crystal structure data for (^{Cl}L)$_2$Ni (CCDC 2044312†). Crystals were grown by slow evaporation of a pentane solution. Red blocks; $C_{44}H_{26}Cl_2N_6Ni$ 768.32 g mol^{-1}, tetragonal, space group $I4_1/a$; $a = b$ = 20.2979(9) Å, c = 39.0458(18) Å, $\alpha = \beta = \gamma$ = 90°, V = 16 087.1(16) $Å^3$; Z = 16, ρ_{calcd} = 1.269 g cm^{-3}; crystal dimensions 0.270 × 0.180 × 0.140 mm; $2\theta_{max}$ = 50.000°; 183 624 reflections, 7058 independent (R_{int} = 0.0960), intrinsic phasing; absorption coeff (μ = 0.653 mm^{-1}), absorption correction semi-empirical from equivalents (SADABS); refinement (against F_o^2) with SHELXTL V6.1, 478 parameters, 0 restraints, R_1 = 0.0592 ($I > 2\sigma$) and wR_2 = 0.1390 (all data), Goof = 1.040, residual electron density 0.65/−0.84 $Å^{-3}$. Several pentane solvent molecules were found to be disordered and could not be modeled successfully. The SQUEEZE protocol embedded in PLATON software was used to mask four solvent voids of 899 $Å^3$ containing 215 e^- each.

Computational methods

All calculations were performed using Gaussian 16, Rev. B01 (ref. 44) with unrestricted Kohn–Sham DFT (UKS), unless otherwise mentioned, and the solvent-model based on density (SMD, solvent = CH_3CN) to account for implicit-solvent effects.[45] Ground triplet state geometries for (^{CF3}L)$_2$Ni and (^{Cl}L)$_2$Ni were optimized with the O3LYP functional[46] and 6-31+G(d,p) basis sets on all atoms.[47–51] Restricted open-shell DFT (ROKS) single point calculation, with the PBE0 functional[52] and the 6-31+G(d,p) basis set on all atoms, at the optimized triplet ground state geometry of (^{CF3}L)$_2$Ni was performed to maximally pair the α- and β-electrons and determine the relative energies of the MOs. Time-dependent DFT (TDDFT) calculations were carried out with the same PBE0 functional and the 6-31+G(d,p) basis set on all atoms on (^{CF3}L)$_2$Ni and (^{Cl}L)$_2$Ni. Ground state molecular orbital (isosurface value = 0.04) and spin density isosurfaces (isosurface value = 0.004) were generated using Gaussview,[53] while electron-hole density maps of select excited states (isosurface value = 0.002) were generated using Multiwfn.[54] TDDFT calculated vertical excitations (f > 0.05) and simulated spectra (FWHM = 3000 cm^{-1}) were generated with GaussSum.[55]

Author contributions

JDB and DEH conceived of the project. JDB conducted all experimental work. IBL carried out computational analysis. MS and JvL conducted magnetism experiments. JDB, IBL and DEH analysed all data. The manuscript was written through contributions of all authors. All authors have given approval to the final version of the manuscript.

Conflicts of interest

There are no conflicts to declare.

Acknowledgements

We gratefully acknowledge the Natural Sciences Engineering Research Council of Canada for a Discovery Grant to D. E. H. (RGPIN-2014-03733) and J. v. L. (NSERC RGPIN-2018-05012); the Canadian Foundation for Innovation and Research Manitoba for an award in support of an X-ray diffractometer (CFI #32146); the University of Manitoba for the Bert & Lee Friesen Graduate Scholarship (I. B. L.) and GETS/SEGS support (J. D. B., I. B. L.); and Compute Canada for access to computational resources. Prof. Viktor N. Nemykin is thanked for access to spectroelectrochemical equipment and helpful discussions.

References

1 P. J. Chirik, *Inorg. Chem.*, 2011, **50**, 9737–9740.
2 W. Kaim, *Inorg. Chem.*, 2011, **50**, 9752–9765.
3 V. Lyaskovskyy and B. de Bruin, *ACS Catal.*, 2012, **2**, 270–279.
4 O. R. Luca and R. H. Crabtree, *Chem. Soc. Rev.*, 2013, **42**, 1440–1459.
5 S. K. Larsen and C. G. Pierpont, *J. Am. Chem. Soc.*, 1988, **110**, 1827–1832.
6 E. P. Ivakhnenko, A. G. Starikov, V. I. Minkin, K. A. Lyssenko, M. Yu. Antipin, V. I. Simakov, M. S. Korobov, G. S. Borodkin and P. A. Knyazev, *Inorg. Chem.*, 2011, **50**, 7022–7032.
7 R. Gross and W. Kaim, *Inorg. Chem.*, 1987, **26**, 3596–3600.
8 T. Büttner, J. Geier, G. Frison, J. Harmer, C. Calle, A. Schweiger, H. Schönberg and H. Grützmacher, *Science*, 2005, **307**, 235–238.
9 E. T. Hennessy and T. A. Betley, *Science*, 2013, **340**, 591.
10 K. Ray, T. Petrenko, K. Wieghardt and F. Neese, *Dalton Trans.*, 2007, 1552–1566.
11 W. Kaim, *Coord. Chem. Rev.*, 2019, **255**, 2503–2513.
12 J. J. Davidson, J. C. DeMott, C. Douvris, C. M. Fafard, N. Bhuvanesh, C.-H. Chen, D. E. Herbert, C.-I. Lee, B. J. McCulloch, B. M. Foxman and O. V. Ozerov, *Inorg. Chem.*, 2015, **54**, 2916–2935.
13 A. Rajput, A. K. Sharma, S. K. Barman, D. Koley, M. Steinert and R. Mukherjee, *Inorg. Chem.*, 2014, **53**, 36–48.
14 T. Storr and R. Mukherjee, *Inorg. Chem.*, 2018, **57**, 9577–9579.
15 K. Hanson, L. Roskop, P. I. Djurovich, F. Zahariev, M. S. Gordon and M. E. Thompson, *J. Am. Chem. Soc.*, 2010, **132**, 16247–16255.
16 P. Mandapati, P. K. Giesbrecht, R. L. Davis and D. E. Herbert, *Inorg. Chem.*, 2017, **56**, 3674–3685.
17 P. Mandapati, J. D. Braun, C. Killeen, R. L. Davis, J. A. G. Williams and D. E. Herbert, *Inorg. Chem.*, 2019, **58**, 14808–14817.
18 P. Mandapati, J. D. Braun, I. B. Lozada, J. A. G. Williams and D. E. Herbert, *Inorg. Chem.*, 2020, **59**, 12504–12517.
19 J. D. Braun, I. B. Lozada, C. Kolodziej, C. Burda, K. M. E. Newman, J. van Lierop, R. L. Davis and D. E. Herbert, *Nat. Chem.*, 2019, **11**, 1144–1150.
20 J. D. Braun, I. B. Lozada and D. E. Herbert, *Inorg. Chem.*, 2020, **59**, 17746–17757.
21 B. Garreau-de Bonneval, K. I. M.-C. Ching, F. Alary, T.-T. Bui and L. Valade, *Coord. Chem. Rev.*, 2010, **254**, 1457–1467.
22 N. D. Fenton and M. Gerloch, *Inorg. Chem.*, 1990, **29**, 3726–3733.
23 M. V. Andreocci, G. Mattogno, R. Zanoni, P. Giannoccaro and G. Vasapollo, *Inorg. Chim. Acta*, 1982, **63**, 225–231.
24 E. A. Makarova, Y. V. Zatsikha, K. M. E. Newman, V. K. Paidi, V. A. Beletsky, J. van Lierop, E. A. Lukyanets and V. N. Nemykin, *Inorg. Chem.*, 2017, **56**, 6052–6055.
25 E. Salojärvi, A. Peuronen, M. Lahtinen, H. Huhtinen, L. S. Vlasenko, M. Lastusaari and A. Lehtonen, *Molecules*, 2020, **25**, 2531.
26 B. J. Liddle, S. Wanniarachchi, J. S. Hewage, S. V. Lindeman, B. Bennett and J. R. Gardinier, *Inorg. Chem.*, 2012, **51**, 12720–12728.
27 J. S. Hewage, S. Wanniarachchi, T. J. Morin, B. J. Liddle, M. Banaszynski, S. V. Lindeman, B. Bennett and J. R. Gardinier, *Inorg. Chem.*, 2014, **53**, 10070–10084.
28 R. Mondal, P. K. Giesbrecht and D. E. Herbert, *Polyhedron*, 2016, **108**, 156–162.
29 P. Mandapati, J. D. Braun, B. K. Sidhu, G. Wilson and D. E. Herbert, *Organometallics*, 2020, **39**, 1989–1997.
30 A. F. Wells, *Structural Inorganic Chemistry*, Clarendon Press; Oxford University Press, Oxford, 5th edn, 1984.
31 D. H. McDaniel and H. C. Brown, *J. Org. Chem.*, 1958, **23**, 420–427.
32 H. Basch, A. Viste and H. B. Gray, *J. Chem. Phys.*, 1966, **44**, 10–19.
33 M. Parthey and M. Kaupp, *Chem. Soc. Rev.*, 2014, **43**, 5067–5088.
34 F. Thomas, *Dalton Trans.*, 2016, **45**, 10866–10877.
35 R. A. Marcus and N. Sutin, *Biochim. Biophys. Acta*, 1985, **811**, 265–322.
36 N. S. Hush, *Prog. Inorg. Chem.*, 1967, **8**, 391–444.
37 P. Zanello, F. Fabrizi de Biani and C. Nervi, in *Inorganic Electrochemistry*, Royal Society of Chemistry, Cambridge, 2007, pp. 159–216.
38 B. L. Westcott, N. E. Gruhn, L. J. Michelsen and D. L. Lichtenberger, *J. Am. Chem. Soc.*, 2000, **122**, 8083–8084.
39 G. A. Bain and J. F. Berry, *J. Chem. Educ.*, 2008, **85**, 532.
40 W. Dohle, A. Staubitz and P. Knochel, *Chem.–Eur. J.*, 2003, **9**, 5323–5331.
41 G. M. Sheldrick, *Acta Crystallogr., Sect. A: Found. Crystallogr.*, 2008, **64**, 112–122.
42 O. V. Dolomanov, L. J. Bourhis, R. J. Gildea, J. A. K. Howard and H. Puschmann, *J. Appl. Crystallogr.*, 2009, **42**, 339–341.
43 A. L. Spek, *Acta Crystallogr., Sect. D: Biol. Crystallogr.*, 2009, **65**, 148–155.
44 M. J. Frisch, G. W. Trucks, H. B. Schlegel, G. E. Scuseria, M. A. Robb, J. R. Cheeseman, G. Scalmani, V. Barone, G. A. Petersson, H. Nakatsuji, X. Li, M. Caricato, A. V. Marenich, J. Bloino, B. G. Janesko, R. Gomperts,

B. Mennucci, H. P. Hratchian, J. V. Ortiz, A. F. Izmaylov, J. L. Sonnenberg, D. Williams-Young, F. Ding, F. Lipparini, F. Egidi, J. Goings, B. Peng, A. Petrone, T. Henderson, D. Ranasinghe, V. G. Zakrzewski, J. Gao, N. Rega, G. Zheng, W. Liang, M. Hada, M. Ehara, K. Toyota, R. Fukuda, J. Hasegawa, M. Ishida, T. Nakajima, Y. Honda, O. Kitao, H. Nakai, T. Vreven, K. Throssell, J. A. Montgomery, J. E. Peralta, F. Ogliaro, M. J. Bearpark, J. J. Heyd, E. N. Brothers, K. N. Kudin, V. N. Staroverov, T. A. Keith, R. Kobayashi, J. Normand, K. Raghavachari, A. P. Rendell, J. C. Burant, S. S. Iyengar, J. Tomasi, M. Cossi, J. M. Millam, M. Klene, C. Adamo, R. Cammi, J. W. Ochterski, R. L. Martin, K. Morokuma, O. Farkas, J. B. Foresman and D. J. Fox, *Gaussian 16, Revision B.01*, Gaussian, Inc., Wallingford CT, 2016.

45 A. V. Marenich, C. J. Cramer and D. G. Truhlar, *J. Phys. Chem. B*, 2009, **113**, 6378–6396.

46 A. J. Cohen and N. C. Handy, *Mol. Phys.*, 2001, **99**, 607–615.

47 R. Ditchfield, W. J. Hehre and J. A. Pople, *J. Chem. Phys.*, 1971, **54**, 724–728.

48 W. J. Hehre, R. Ditchfield and J. A. Pople, *J. Chem. Phys.*, 1972, **56**, 2257–2261.

49 P. C. Hariharan and J. A. Pople, *Theor. Chim. Acta*, 1973, **28**, 213–222.

50 T. Clark, J. Chandrasekhar, G. W. Spitznagel and P. v. R. Schleyer, *J. Comput. Chem.*, 1983, **4**, 294–301.

51 V. A. Rassolov, J. A. Pople, M. A. Ratner and T. L. Windus, *J. Chem. Phys.*, 1998, **109**, 1223–1229.

52 C. Adamo and V. Barone, *J. Chem. Phys.*, 1999, **110**, 6158–6170.

53 R. Dennington, T. A. Keith and J. M. Millam, *GaussView, Version 6*, Semichem Inc., Shawnee Mission, KS, 2016.

54 T. Lu and F. Chen, *J. Comput. Chem.*, 2012, **33**, 580–592.

55 N. M. O'Boyle, A. L. Tenderholt and K. M. Langner, *J. Comput. Chem.*, 2008, **29**, 839–845.